JACS
JOURNAL OF THE AMERICAN CHEMICAL SOCIETY
pubs.acs.org/JACS
Article

Intrareticular Energy Transfer in Dual-Photosensitized Metal–Organic Frameworks to Enhance Photoelectrochemical Performance

Weisu Kong, Tianrui Liu, Xiaoxiao Meng, Pengfei Dong, Jianping Lei, and Huangxian Ju*

Cite This: *J. Am. Chem. Soc.* 2025, 147, 24976–24983
Read Online

ACCESS | Metrics & More | Article Recommendations | Supporting Information

ABSTRACT: Metal–organic frameworks (MOFs) have garnered significant interest in photoelectrochemistry (PEC). To overcome the intrinsic drawbacks of narrow-wavelength absorption and limited photon utilization, this study used two photosensitizers as hybrid ligands to realize intrareticular energy transfer (IRET) and multiple wavelength light absorption for enhancing photoelectrochemical performance. The dual-photosensitized MOF (dpMOF) contained a $[Cd_2(COO)_4]$ paddlewheel unit as the metal node along with meso-tetra(4-carboxyphenyl)porphine and pyridine-functionalized boron dipyrromethene ligands serving as the energy acceptor and donor units, respectively. Both experimental data and theoretical calculations confirmed the energy transfer. The IRET process possessed an energy transfer efficiency of up to 88.3%, significantly promoting photon utilization and charge separation. Compared with single photosensitized MOFs with similar topologies, IRET in dpMOF resulted in 2.6–6.5 times enhanced photocurrent under multiple wavelength irradiation. Therefore, an advanced PEC biosensing strategy was proposed to demonstrate the PEC application of dpMOF. This work offers new insights into the design of enhanced MOFs and photoconversion applications.

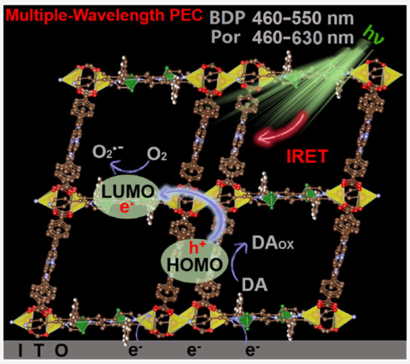

Downloaded via NANJING UNIV on July 23, 2025 at 03:05:50 (UTC).
See https://pubs.acs.org/sharingguidelines for options on how to legitimately share published articles.

INTRODUCTION

The light absorption, energy conversion, and carrier photogeneration capability of photoactive materials are crucial for enhancing their photon utilization and photoelectrochemical (PEC) performance.[1−4] However, most developed photoactive semiconductors, such as metal oxides/sulfides,[5,6] organic small molecules,[7] polymers,[8] and quantum dots (QDs),[9,10] suffer from narrow visible light absorption range, low photon utilization, and ill-defined photoelectron transfer paths. These intrinsic drawbacks significantly suppress PEC performance. Therefore, the breakthrough in PEC technology requires the rational design of photoactive materials to address these critical issues. For example, the stepwise assembly of QDs and photoactive dyes has been used to broaden the visible light absorption range,[11] and a deficient ternary metal sulfide ($CdIn_2S_4$) photoanode has been designed to enhance the photon-to-current efficiency.[12] Although the integration of photoactive materials can satisfy the requirements for widening the wavelength range of light absorption, the complex compositional design limits flexibility in material selection. Hence, it is essential to develop multifunctional semiconductor materials with precise structures and convenient preparation processes.

Metal–organic frameworks (MOFs) are a class of porous materials with periodic structures[13−16] and have attracted extensive research interest in PEC fields. A host–guest MOF has been designed to facilitate photogenerated exciton type conversion by efficiently transferring energy from the MOF skeleton to molecular acceptors.[17] Recently, our group[18] also developed an electron donor-coordinated MOF to enhance the PEC performance by shortening the charge transfer pathway. However, the limited light energy utilization of MOFs currently restricts improvement in PEC performance. Considering that the high efficiency of long-distance and directional energy transfer (ET) in photosynthesis is mainly attributed to highly ordered chlorophylls (porphyrin-like pigments),[19] MOFs with ordered porphyrins have been proposed as highly efficient light harvesting and ET components to boost photocatalytic activity.[20] Indeed, the covalent combination of porphyrin and boron dipyrromethene derivatives significantly extends the light absorption range and has successfully achieved intermolecular ET to promote photon harvesting.[21−23] However, the inherent defects of organic small molecules in these MOF structures, such as instability and low carrier mobility,[24] limit their application in PEC fields.

To boost the light absorption, facilitate the photoelectric conversion, and improve the charge-carrier mobility, this work

Received: May 7, 2025
Revised: June 23, 2025
Accepted: June 27, 2025
Published: July 2, 2025

© 2025 American Chemical Society

https://doi.org/10.1021/jacs.5c07699

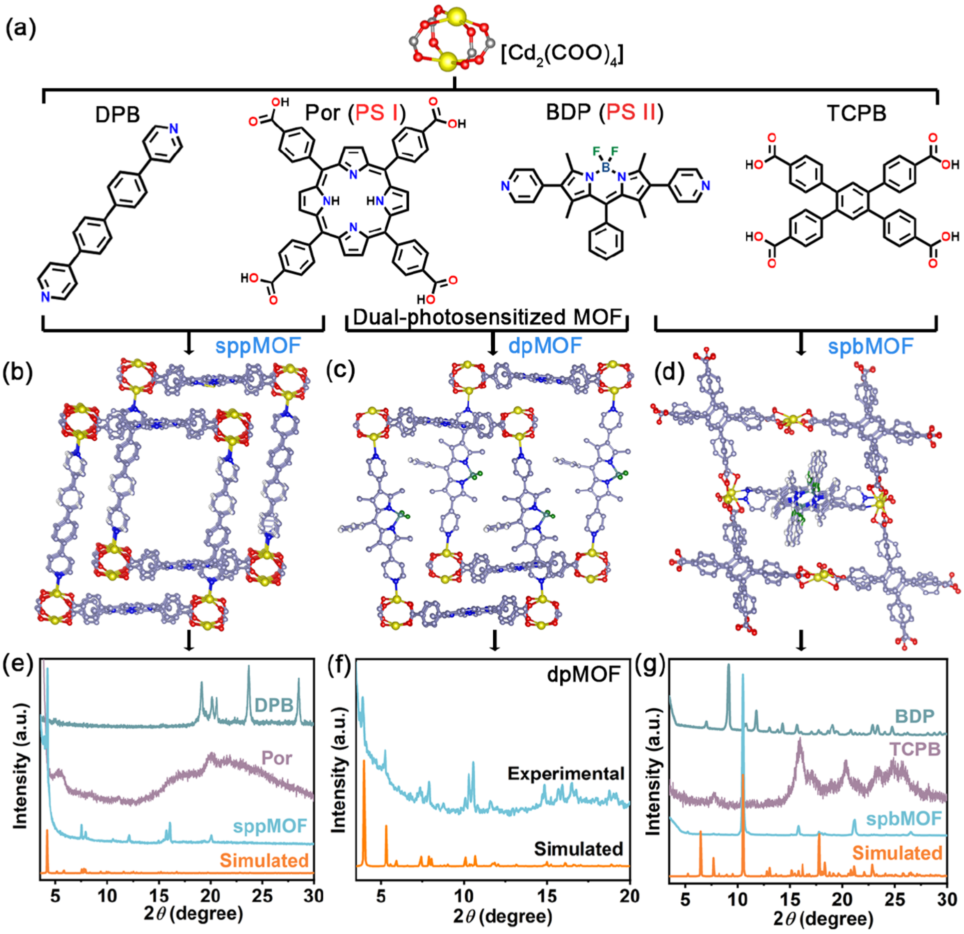

Figure 1. (a) Structures of building blocks: [$Cd_2(COO)_4$] paddlewheel unit, DPB, Por, BDP, and TCPB ligands. C, gray; O, red; N, blue; Cd, yellow. (b–d) Topology network structures of sppMOF, dpMOF, and spbMOF. (e–g) PXRD patterns of sppMOF, DPB, Por, dpMOF, spbMOF, BDP, and TCPB.

designed an intrareticular ET (IRET) strategy by integrating the structural advantages of multicomponent MOFs to synthesize a novel dual-photosensitized MOF (dpMOF). Two photosensitizers, meso-tetra(4-carboxyphenyl)porphine (Por) and pyridine-functionalized boron dipyrromethene (BDP), as hybrid ligands of the metal node of [$Cd_2(COO)_4$] paddlewheel unit (Figure 1a) could act as the energy acceptor and donor for IRET, respectively, after the BDP ligand absorbed the light irradiation from 460 to 550 nm. Compared with the single photosensitized MOFs, sppMOF, and spbMOF prepared with nonphotosensitized small molecule organic ligands 4,4′-di(4-pyridyl)biphenyl (DPB) and 1,2,4,5-tetrakis(4-carboxyphenyl) benzene (TCPB) to replace BDP and Por, respectively, IRET in dpMOF demonstrated a photocurrent enhancement of 2.6–6.5 folds under multiple wavelength irradiation. The role of IRET in enhancing PEC performance was well demonstrated by experiments and density functional theory (DFT) calculations. Especially, the IRET process promoted photon utilization and charge-carrier mobility, and the energy transfer efficiency was up to 88.3% under 545 nm irradiation. The excellent PEC performance of dpMOF was also used for sensitive biosensing of vascular endothelial growth factor 165 ($VEGF_{165}$), a protein that plays a critical role in angiogenesis. Overall, the design of dpMOF with a broad absorption range provides a proof of concept to construct reliable IRET for enhancing the PEC performance of MOFs and expanding the photoconversion applications.

■ RESULTS AND DISCUSSION

Design and Synthesis of MOFs. The single crystal of dpMOF was prepared with the synthesized Por and BDP (Figures S1–S5) as ligands via a solvothermal method, while sppMOF and spbMOF were obtained by replacing BDP and Por with DPB and TCPB, respectively (Figure 1a). Single-crystal X-ray diffraction (XRD) and crystal analysis provided the corresponding topologies (Figures 1b–d and S6), revealing space groups $P2_1/n$ for dpMOF and spbMOF, and *P-1* for sppMOF (Tables S1–S3). Furthermore, powder XRD (PXRD) measurements confirmed that the synthesized sppMOF, dpMOF, and spbMOF exhibited ideal crystallinity and matched well with the simulated XRD peaks (Figures 1e–g and S7). The diffraction peaks at 4.0, 5.3, 6.0, 7.4, 7.9, 10.1, 10.3, and 10.6° could be indexed to the (002), (10−1), (101), (11−1), (111), (113), (11−4), and (20−2) facets of dpMOF (CCDC deposition number: 2361207), respectively. Transmission electron microscopic (TEM) images characterized their morphologies, which exhibited blocky microstructures (Figure S8) with a homogeneous distribution of Cd, C, N, O, F, and B elements (Figures S9–S11). N_2 adsorption–desorption tests confirmed the porous nature of dpMOF, sppMOF, and spbMOF, and the adsorption isotherms

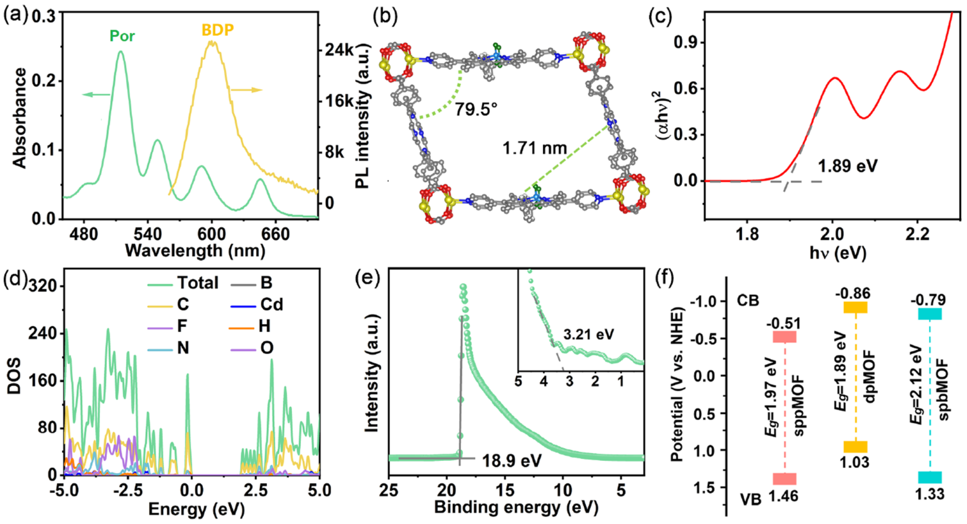

Figure 2. (a) UV−vis absorption spectrum of Por (green) and PL spectrum of BDP (orange yellow). (b) Distance and dihedral angle between proximate Por and BDP ligands in the crystal structure. (c) Tauc plot of dpMOF. (d) DOS curves of dpMOF and its components. (e) UPS of dpMOF. Inset: relative energy gap between the maximum valence band and Fermi level. (f) Valence band (VB) and conduction band (CB) energy levels of sppMOF, dpMOF, and spbMOF.

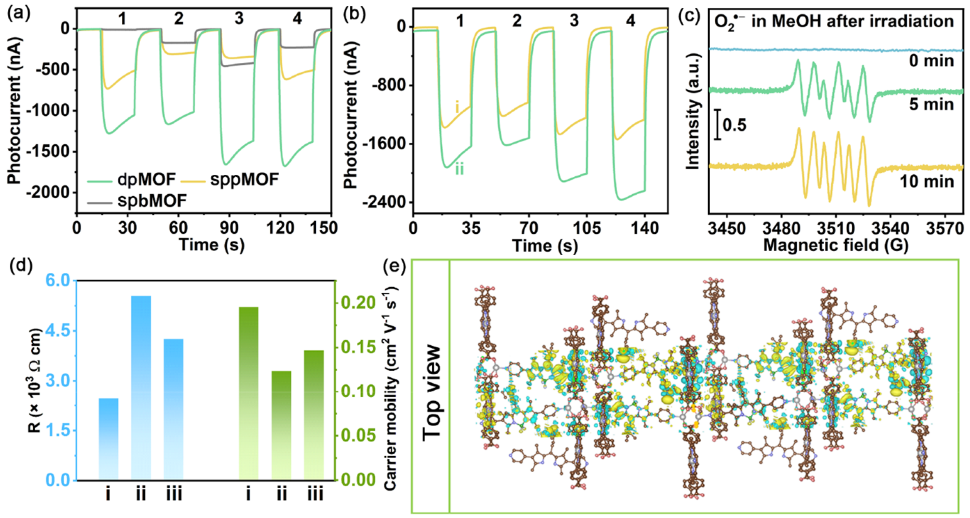

Figure 3. (a, b) Photocurrent−time curves of dpMOF-, sppMOF-, and spbMOF-modified ITO in air-saturated PBS (a), and dpMOF/ITO in air- (i) and O_2-saturated (ii) PBS (b) in the presence of 10 mM DA under light irradiation with wavelengths of 630 (1), 550 (2), 500 (3), and 460 (4) nm. (c) EPR spectra of dpMOF in DMPO methanol solution under Xe lamp irradiation for 0, 5, and 10 min. (d) Electrical resistivity (R) and carrier mobility of dpMOF (i), sppMOF (ii), and spbMOF (iii). (e) Charge density difference between the lowest electron excitation and the original ground state of dpMOF from the top view. Electron density gain and loss are colored yellow and green, respectively.

indicated H_4-type hysteresis loops (Figure S12). The Brunauer−Emmett−Teller surface areas of dpMOF, sppMOF, and spbMOF were simulated to be 226.2, 106.2, and 48.88 m^2 g^{-1}, respectively. Notably, dpMOF exhibited a high specific surface area, favoring to increase the surface redox-active sites.[25] Thermogravimetric analysis further verified the relative contents of different components in MOFs by observing the variation in sample weight with temperature (Figure S13). Overall, the excellent crystallinity verified the successful synthesis of the designed MOFs.

Feasibility of IRET. The ultraviolet−visible (UV−vis) spectrum of dpMOF showed two absorption peaks at 440 and 520 nm, which corresponded to the absorption of the Por ligand with 20 nm red shift compared with pure Por and BDP ligand, respectively, while the UV−vis spectra of sppMOF and spbMOF showed only the absorption peak of Por or BDP ligand (Figure S14), indicating the extended light absorption range of dpMOF. The efficient IRET process between Por and BDP ligands was demonstrated using the absorption spectrum of Por and the photoluminescence (PL) spectrum of BDP (Figure 2a). The spectral overlap of Por absorption and BDP emission in the range of 575−660 nm confirmed the possibility of ET from BDP to Por units. The distance and angle between the two photosensitizers in dpMOF were approximately 1.71 nm and 79.5° (Figure 2b), respectively, proving that IRET between the BDP and Por units belonged to the Förster resonance ET.

Semiconducting Properties and Energy Band Calculations of MOFs. To prove the semiconducting properties of dpMOF, the UV−vis diffuse reflectance spectra (DRS) of dpMOF, sppMOF, and spbMOF were recorded (Figure S15). The absorption peaks of dpMOF were red-shifted compared

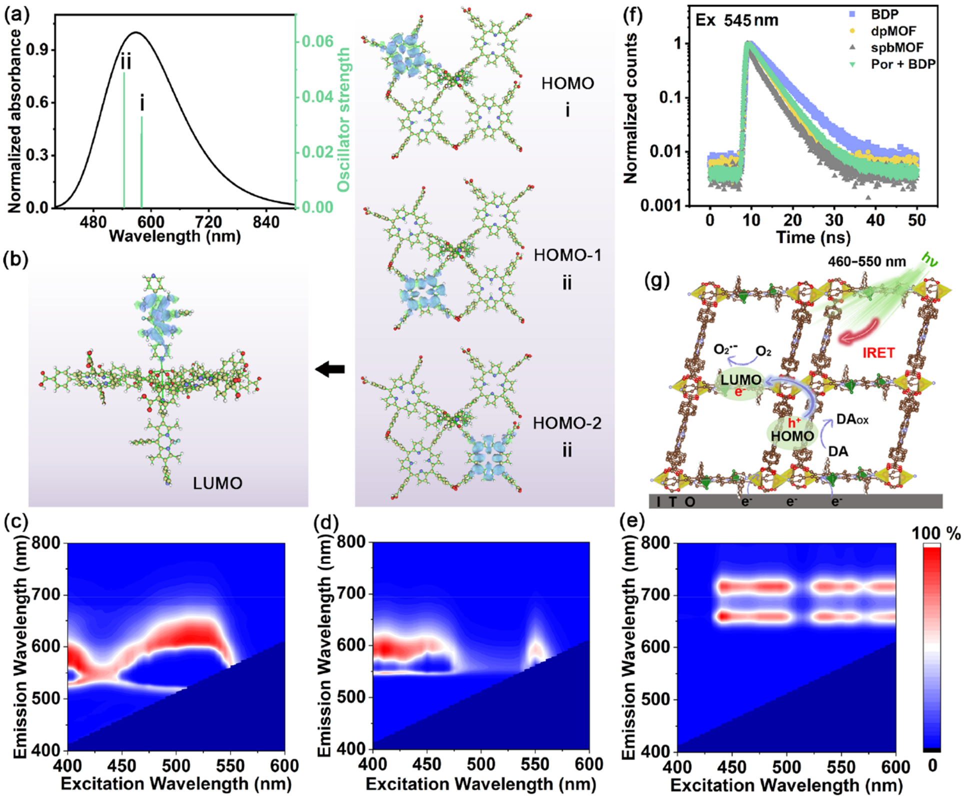

Figure 4. (a) Calculated UV−vis absorption spectrum of dpMOF. (b) MO isodensity surfaces in i and ii absorption bands of dpMOF. Green and blue regions denote the positive and negative orbital phases, respectively (isovalue = 0.01). (c−e) Excitation−emission maps of dpMOF (c), BDP (d), and Por (e). (f) PL lifetime curves of Por, BDP, dpMOF, sppMOF, and pbMOF under 545 nm excitation. (g) A schematic illustration of the PEC process of dpMOF with IRET mechanism in the presence of DA and dissolved O_2.

with BDP and Por ligands, suggesting that intermolecular charge transfer between the BDP and Por ligands occurred in dpMOF. Moreover, the assembly of BDP and Por ligands into dpMOF increased the degree of conjugation of the whole system through $\pi-\pi$ stacking interactions,[20] potentially leading to a red-shifting of absorption peaks. The forbidden bandwidths of dpMOF, sppMOF, and spbMOF were obtained with the Tauc plot method to be 1.89, 1.97, and 2.12 eV, respectively (Figures 2c, S15, and S16),[26] indicating a narrower band gap width (E_g) of dpMOF. The E_g value was slightly lower than the direct band gap width of 2.22 eV obtained by DFT calculation with the density of states (DOS) of dpMOF (Figure 2d). Theoretically, a narrower E_g results in more photogenerated carriers, which is favorable for enhancing the PEC performance.[14,27]

The electronic properties of dpMOF, sppMOF, and spbMOF were investigated using Mott−Schottky curves (Figure S17) and UV photoelectron spectra (UPS, Figures S18 and 2e). The flat band (E_{FB} vs Ag/AgCl) and onset (E_{onset}) potentials were measured at −0.16 and 18.90 eV for dpMOF, −0.30 and 19.08 eV for sppMOF, and −0.22 and 19.16 eV for spbMOF, respectively. Their relative electronic binding energies between the valence band maximum (E_{VBM}) and Fermi energy level were found to be 3.21, 3.82, and 3.77 eV, respectively. According to the work function formula,[28−30] the E_{VBM} of dpMOF, sppMOF, and spbMOF was calculated to be −5.53, −5.96, and −5.83 eV for dpMOF, sppMOF, and spbMOF, respectively. Thus, the conduction band minimum (E_{CBM}) could be obtained with $E_g = E_{CBM} - E_{VBM}$,[31] as depicted in Figure 2f. The more negative conduction band (CB) energy level of dpMOF indicated its stronger reducing ability,[32] which was favorable for generating photoelectrons.

PEC Characterization of MOFs. The photoinduced electron transfer ability of dpMOF was verified by PEC measurements (Figure 3a). In comparison with sppMOF- and spbMOF-modified indium tin oxide (ITO) electrodes, the dpMOF-modified ITO electrode prepared with the optimal amount of dpMOF (Figure S19) exhibited the highest photocurrent response under light irradiation at individual wavelengths. The photocurrent at 630 nm irradiation (Figures 3a and S20a) was mainly attributed to the response of the Por ligand with the $\pi-\pi$ stacking effect that facilitated framework electron transfer,[20,33] which was not further studied in this work. The photocurrent responses under irradiation at 460, 550, and 500 nm could be attributed to the IRET process from BDP to Por ligands (Figures S14 and S20a). The photocurrents of dpMOF were 2.6−3.6 and 4.2−6.5 times those of sppMOF and spbMOF, respectively (Figure S21 and Table S4). In contrast, the photocurrent responses were very weak in the absence of a photosensitive ligand, approaching those of bare ITO under light irradiation (Figures S20b and S22). Thus, the presence of IRET in dpMOF greatly improved its PEC performance. Moreover, the PEC intensity of dpMOF remained stable after continuous irradiation for over 2000 s (Figure S23), indicating the excellent PEC performance of dpMOF.

To perform the PEC analysis, the detection solution usually contains an electron sacrifice, such as ascorbic acid or dopamine (DA), to prevent the recombination of electron−hole pairs by consuming the generated holes, which can greatly

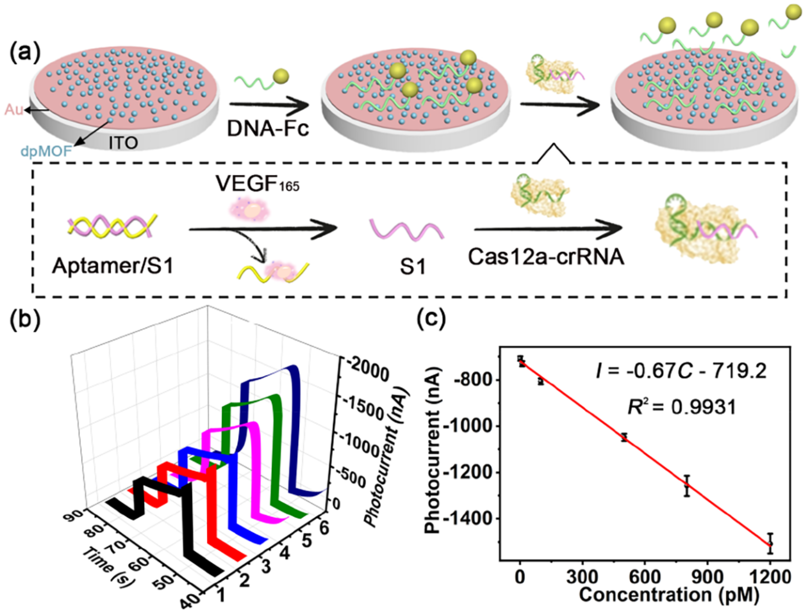

Figure 5. (a) Schematic diagram of PEC biosensor preparation for $VEGF_{165}$ detection. (b) Photocurrent responses of the biosensor to $VEGF_{165}$ in the range of 1, 10, 100, 500, 800, and 1200 pM (from 1 to 6) in 0.1 M PBS containing 0.1 M NaCl and 10 mM DA under light irradiation of 500 nm. (c) The corresponding calibration curve for $VEGF_{165}$ determination.

increase the photocurrent (Figure S24). Furthermore, the photocurrent of dpMOF/ITO significantly depended on the presence of dissolved oxygen (Figures S25 and 3b), demonstrating the transfer of generated photoelectrons to O_2, which produced $O_2^{\bullet-}$. This phenomenon was supported by the more negative CB potential (−0.86 V vs NHE) of dpMOF than the reduction potential of −0.33 V (vs NHE) for $O_2/O_2^{\bullet-}$.[34]

PEC Mechanism of dpMOF. To verify the generation of $O_2^{\bullet-}$ in the PEC process, electron paramagnetic resonance (EPR) spectra of dpMOF, sppMOF, and spbMOF were recorded in 5,5-dimethyl-1-pyrroline N-oxide (DMPO) methanol solutions under light irradiation for different times,[35] which revealed the increasing characteristic signals of DMPO-$O_2^{\bullet-}$ (Figures 3c and S26). Thus, the photocathode currents generated by the three MOFs could be attributed to photogenerated electron migration to their surface to reduce O_2. Meanwhile, the Hall effect (Figure 3d and Table S5) confirmed that dpMOF possessed a higher carrier mobility and lower resistivity. The electron transfer process in dpMOF was demonstrated with DFT calculations, which illustrated the charge density difference between the lowest electronically excited state and the original ground state of dpMOF (Figures 3e and S27), and indicated the electron loss from the Por ligand and the electron gain by the BDP ligand. The efficient electron transfer process between the two ligands promoted photon utilization and improved PEC performance.

The separation of electron−hole pairs and electron transfer between the two ligands were further verified with time-dependent DFT calculations. The theoretical simulated UV−vis absorption spectra revealed multiple detectable absorption bands of Por and BDP (Figure S28). Specifically, Por exhibited the absorption peaks at 428.1, 431.0, 555.5, and 587.1 nm corresponding to transitions from the ground state (S_0) to excited states (S_1−S_4), respectively (Figure S29), and BDP showed only one absorption peak at 460.2 nm corresponding to the S_0 to S_1 transition (Figure S30). Similarly, dpMOF displayed two detectable absorption bands (Figure 4a) at 543.6 and 580.5 nm. The latter corresponded to the highest occupied molecular orbital (HOMO) of Por ligand to its lowest unoccupied molecular orbital (LUMO) transition (i), and the former could be attributed to the transitions from excited states HOMO−1 and HOMO−2 of Por ligand to LUMO of BDP ligand (ii), indicating the electron transfer between two ligands. Oscillator-based intensities also verified that the main contribution of excited states of dpMOF was due to the HOMO−1/−2 to LUMO transitions (Figure 4b and Table S6), confirming the separation of electron−hole pairs within the framework. To further evaluate the energy transfer process of dpMOF, it was verified using three-dimensional (3D) fluorescence spectra of the sample. dpMOF exhibited a robust emission peak of the BDP ligand at 520−650 nm (Figure 4c,d), while the emission peaks of the Por ligand at 655 and 720 nm almost disappeared (Figure 4e), which was mainly attributed to ET from BDP to Por ligand in dpMOF. Furthermore, the 3D fluorescence map of the mixed ligand spbMOF with a single photosensitizer corresponded to the BDP ligand, whereas there was a clear weakening of the fluorescence of sppMOF (Figure S31). To further explore the contribution of IRET in dpMOF to PEC performance, the IRET efficiency (E_{IRET}) was evaluated by time-resolved photoluminescence (Figures 4f and S32, Table S7) and quantum yield (ψ, Figures S33, S34, and Table S8) measurements.[36−38] Taking 545 nm excitation as an example, ψ_{dpMOF}, ψ_{Por}, ψ_{BDP}, and PL lifetime of dpMOF were 6.96, 7.2, 59.5%, and 3.69 ns, respectively, and the IRET rate from BDP to Por was calculated to be 1.47×10^{-9} s^{-1} with an 88.3%. The results demonstrated that the fast energy transfer led to a lower PL lifetime of dpMOF, which accelerated electron transfer. Notably, the energy conversion efficiency was higher than 65−71% of other Por-derived MOFs[39−41] and 60% of BDP-based MOF,[42] suggesting greater potential of dpMOF for efficient light harvesting. Furthermore, dpMOF(Ni) obtained by doping Ni into dpMOF (Figures S35 and S36) was used to investigate the interaction between ligands and metal nodes. dpMOF exhibited a much higher photocurrent than both dpMOF(Ni) (Figure S37) and a single photosensitizer Por-based MOF (Figure S38). The enhancement could be attributed to two factors: (1) the arrangement of electrons on the d-orbitals of the Ni^{2+} node (Figure S39), which made it more receptive to accepting electrons from the ligand, suggesting that a stronger ligand-to-metal charge transfer was unfavorable for improving the PEC performance; (2) the synergistic interaction between dual photosensitizing components in dpMOF, which collectively boosted photoelectrochemical activity. In light of the experimental and DFT computational investigations described above, a mechanism through which IRET augments charge separation within dpMOFs is proposed in Figure 4g. After light irradiation and IRET, the photoelectrons generated from Por ligands were transferred to LUMO of BDP ligands and then O_2 to form $O_2^{\bullet-}$, which produced the photocurrent. At low pH, the photocurrent was greater due to the protonation of the oxidized $O_2^{\bullet-}$ (Figure S40). Meanwhile, DA, as an electron donor, was oxidized by the photogenerated holes to maintain charge balance in the framework.

PEC Biosensing Application. To verify the application potential of dpMOF, a PEC detection method was proposed by combining the trans-cleavage function of Cas12a-crRNA with the gold film deposited dpMOF/ITO electrode (Au/dpMOF/ITO), which was modified with DNA-ferrocene (Fc) as a biosensor (Figure 5a). Here, Fc acted as an electron quencher after it donated electrons to the hole,[43] which led to a photocurrent decrease of Au/dpMOF/ITO (Figure S41). Using $VEGF_{165}$ as a target analyte, an assistant probe was prepared by hybridizing its aptamer and a specific DNA sequence (S1). After $VEGF_{165}$ was incubated with the probe to release S1 (Figure S42), the trans-cleavage function of Cas12a-crRNA was activated by binding the released S1 to cleave the DNA-Fc on the biosensor, which led to the increased photocurrent. Similarly, EIS measurements validated the successful assembly of the sensor platform (Figure S43). Under optimal conditions (Figure S44), the photocurrent under 500 nm light irradiation showed a linear increase upon the increasing $VEGF_{165}$ concentration from 1 to 1200 pM (Figure 5b,c). The detection limit at $S/N = 3$ was 0.43 pM, which was lower compared with the fluorescence and electrochemical methods (Table S9).[44,45] Although previous PEC and electrochemiluminescence methods developed for $VEGF_{165}$ detection achieved lower detection limits, they involved long time enzyme-assisted cyclic amplification on biosensor surface,[46,47] and complex aptasensor fabrication and low accuracy.[48] The detection of different proteins and serum samples demonstrated good specificity (Figure S45) and accuracy (Table S10). Hence, the designed IRET strategy and proposed dpMOF possess good prospects in PEC biosensing and photoconversion applications.

CONCLUSIONS

This study synthesized a dual-photosensitized MOF to achieve the designed IRET strategy and enhance the PEC performance of MOFs. dpMOF with excellent crystallinity could be conveniently synthesized with $[Cd_2(COO)_4]$ as a metal node and two photosensitizers as ligands, BDP acted as both light absorption ligand and energy donor, and Por served as an energy acceptor. Both the experimental verifications and DFT calculations confirmed the IRET process from BDP to Por ligands in the MOF skeleton, which resulted in the separation of electron−hole pairs to generate the photoelectrons from Por ligands and then the electron transfer from HOMO−1/−2 of Por ligands to LUMO of BDP ligands. The IRET efficiency of up to 88.3% greatly enhanced the PEC performance with a photocurrent increase by 2.6−6.5 times. The practical applications of the interligand IRET were demonstrated with a proposed PEC method for convenient and sensitive detection of protein. This study not only provides new insights into the development of photoactive materials with high photon utilization but also expands the application of MOFs in PEC bioanalysis and photoconversion.

ASSOCIATED CONTENT

Supporting Information

The Supporting Information is available free of charge at https://pubs.acs.org/doi/10.1021/jacs.5c07699.

> Materials and methods, detailed synthesis and additional characterization of the obtained MOFs, PEC tests, sensing platform assembly, optimization of experimental conditions, and DFT calculations (PDF)

Accession Codes

Deposition Numbers 2361207, 2361279, and 2361317 contain the supplementary crystallographic data for this paper. These data can be obtained free of charge via the joint Cambridge Crystallographic Data Centre (CCDC) and Fachinformationszentrum Karlsruhe Access Structures service.

AUTHOR INFORMATION

Corresponding Author

Huangxian Ju − *State Key Laboratory of Analytical Chemistry for Life Science, School of Chemistry and Chemical Engineering, Nanjing University, Nanjing 210023, P. R. China*; orcid.org/0000-0002-6741-5302; Email: hxju@nju.edu.cn

Authors

Weisu Kong − *State Key Laboratory of Analytical Chemistry for Life Science, School of Chemistry and Chemical Engineering, Nanjing University, Nanjing 210023, P. R. China*

Tianrui Liu − *State Key Laboratory of Analytical Chemistry for Life Science, School of Chemistry and Chemical Engineering, Nanjing University, Nanjing 210023, P. R. China*

Xiaoxiao Meng − *State Key Laboratory of Analytical Chemistry for Life Science, School of Chemistry and Chemical Engineering, Nanjing University, Nanjing 210023, P. R. China*

Pengfei Dong − *State Key Laboratory of Analytical Chemistry for Life Science, School of Chemistry and Chemical Engineering, Nanjing University, Nanjing 210023, P. R. China*

Jianping Lei − *State Key Laboratory of Analytical Chemistry for Life Science, School of Chemistry and Chemical Engineering, Nanjing University, Nanjing 210023, P. R. China*; orcid.org/0000-0002-3594-180X

Complete contact information is available at: https://pubs.acs.org/10.1021/jacs.5c07699

Author Contributions

All authors have approved the final version of the manuscript.

Notes

The authors declare no competing financial interest.

ACKNOWLEDGMENTS

This work was financially supported by the National Natural Science Foundation of China (21827812 and 21890741) and the Science and Technology Project of Nanjing City (202110023).

REFERENCES

(1) Yang, M. Y.; Zhang, S. B.; Zhang, M.; Li, Z. H.; Liu, Y. F.; Liao, X.; Lu, M.; Li, S. L.; Lan, Y. Q. Three-Motif Molecular Junction Type Covalent Organic Frameworks for Efficient Photocatalytic Aerobic Oxidation. *J. Am. Chem. Soc.* **2024**, *146*, 3396−3404.

(2) Li, S.; Li, L.; Li, Y.; Dai, L.; Liu, C.; Liu, Y.; Li, J.; Lv, J.; Li, P.; Wang, B. Fully Conjugated Donor−Acceptor Covalent Organic Frameworks for Photocatalytic Oxidative Amine Coupling and Thioamide Cyclization. *ACS Catal.* **2020**, *10*, 8717−8726.

(3) Yang, W.; Prabhakar, R. R.; Tan, J.; Tilley, S. D.; Moon, J. Strategies for Enhancing the Photocurrent, Photovoltage, and Stability of Photoelectrodes for Photoelectrochemical Water Splitting. *Chem. Soc. Rev.* **2019**, *48*, 4979−5015.

(4) Wu, H.; Tan, H. L.; Toe, C. Y.; Scott, J.; Wang, L.; Amal, R.; Ng, Y. H. Photocatalytic and Photoelectrochemical Systems: Similarities and Differences. *Adv. Mater.* **2020**, *32*, No. 1904717.

(5) Zhou, Y.; Yin, H.; Ai, S. Applications of Two-Dimensional Layered Nanomaterials in Photoelectrochemical Sensors: A Comprehensive Review. *Coordin. Chem. Rev.* **2021**, *447*, No. 214156.

(6) Zhang, B.; An, Z.; Li, M.; Guo, L. H. Synthesis, Functionalization and Photoelectrochemical Immunosensing Application of WO_3-Based Semiconductor Materials. *Trends Anal. Chem.* **2023**, *165*, No. 117149.

(7) Duncan, W. R.; Craig, C. F.; Prezhdo, O. V. Time-Domain ab Initio Study of Charge Relaxation and Recombination in Dye-Sensitized TiO_2. *J. Am. Chem. Soc.* **2007**, *129*, 8528−8543.

(8) Wu, C.; Deng, H.; Ding, Q.; Yuan, R.; Yuan, Y. Au Nano-Flower/Organic Polymer Heterojunction-Based Cathode Photochemical Biosensor with Reduction-Accelerated Quenching Effect of Porphyrin Manganese. *J. Hazard. Mater.* **2023**, *445*, No. 130510.

(9) Sun, W. T.; Yu, Y.; Pan, H. Y.; Gao, X. F.; Chen, Q.; Peng, L. M. CdS Quantum Dots Sensitized TiO_2 Nanotube-Array Photoelectrodes. *J. Am. Chem. Soc.* **2008**, *130*, 1124−1125.

(10) Wang, K.; Wang, C.; Tao, Y.; Tang, Z.; Benetti, D.; Vidal, F.; Liu, Y.; Rummeli, M. H.; Zhao, H.; Rosei, F.; Sun, X. High-Performance Photoelectrochemical Hydrogen Production Using Asymmetric Quantum Dots. *Adv. Funct. Mater.* **2024**, *34*, No. 2400580.

(11) Hao, Q.; Shan, X. N.; Lei, J. P.; Zang, Y.; Yang, Q. H.; Ju, H. X. A Wavelength-Resolved Ratiometric Photoelectrochemical Technique: Design and Sensing Applications. *Chem. Sci.* **2016**, *7*, 774−780.

(12) Wang, H.; Xia, Y.; Li, H.; Wang, X.; Yu, Y.; Jiao, X.; Chen, D. Highly Active Deficient Ternary Sulfide Photoanode for Photoelectrochemical Water Splitting. *Nat. Commun.* **2020**, *11*, No. 3078.

(13) Lee, S. J.; Telfer, S. G. Multicomponent Metal-Organic Frameworks. *Angew. Chem., Int. Ed.* **2023**, *62*, No. e202306341.

(14) Xie, L. S.; Skorupskii, G.; Dinca, M. Electrically Conductive Metal−Organic Frameworks. *Chem. Rev.* **2020**, *120*, 8536−8580.

(15) O'Shaughnessy, M.; Glover, J.; Hafizi, R.; Barhi, M.; Clowes, R.; Chong, S. Y.; Argent, S. P.; Day, G. M.; Cooper, A. I. Porous Isoreticular Non-Metal Organic Frameworks. *Nature* **2024**, *630*, 102−108.

(16) Ding, G.; Li, C.; Chen, L.; Liao, G. Porphyrin-Based Metal−Organic Frameworks for Photo(electro)catalytic CO_2 Reduction. *Energy Environ. Sci.* **2024**, *17*, 5311−5335.

(17) Liang, C.; Cheng, L.; Zhang, S.; Yang, S.; Liu, W.; Xie, J.; Li, M. D.; Chai, Z.; Wang, Y.; Wang, S. Boosting the Optoelectronic Performance by Regulating Exciton Behaviors in a Porous Semiconductive Metal−Organic Framework. *J. Am. Chem. Soc.* **2022**, *144*, 2189−2196.

(18) Kong, W. S.; Zhu, D.; Zhang, Y.; Luo, R. G.; Ma, J.; Lei, J. P.; Ju, H. X. Electron Donor Coordinated Metal-Organic Framework to Enhance Photoelectrochemical Performance. *Angew. Chem., Int. Ed.* **2023**, *62*, No. e202308514.

(19) Son, H. J.; Jin, S.; Patwardhan, S.; Wezenberg, S. J.; Jeong, N. C.; So, M.; Wilmer, C. E.; Sarjeant, A. A.; Schatz, G. C.; Snurr, R. Q.; Farha, O. K.; Wiederrecht, G. P.; Hupp, J. T. Light-Harvesting and Ultrafast Energy Migration in Porphyrin-Based Metal−Organic Frameworks. *J. Am. Chem. Soc.* **2013**, *135*, 862−869.

(20) Huang, Z. W.; Hu, K. Q.; Li, X. B.; Bin, Z. N.; Wu, Q. Y.; Zhang, Z. H.; Guo, Z. J.; Wu, W. S.; Chai, Z. F.; Mei, L.; Shi, W. Q. Thermally Induced Orderly Alignment of Porphyrin Photoactive Motifs in Metal−Organic Frameworks for Boosting Photocatalytic CO_2 Reduction. *J. Am. Chem. Soc.* **2023**, *145*, 18148−18159.

(21) Nikolaou, V.; Charalambidis, G.; Landrou, G.; Nikoloudakis, E.; Planchat, A.; Tsalameni, R.; Junghans, K.; Kahnt, A.; Odobel, F.; Coutsolelos, A. G. Antenna Effect in BODIPY-(Zn)Porphyrin Entities Promotes H_2 Evolution in Dye-Sensitized Photocatalytic Systems. *ACS Appl. Energy Mater.* **2021**, *4*, 10042−10049.

(22) Bucher, L.; Desbois, N.; Harvey, P. D.; Gros, C. P.; Sharma, G. D. Porphyrin Antenna-Enriched BODIPY−Thiophene Copolymer for Efficient Solar Cells. *ACS Appl. Mater. Interfaces* **2018**, *10*, 992−1004.

(23) Lee, C. Y.; Farha, O. K.; Hong, B. J.; Sarjeant, A. A.; Nguyen, S. T.; Hupp, J. T. Light-Harvesting Metal-Organic Frameworks (MOFs): Efficient Strut-to-Strut Energy Transfer in Bodipy and Porphyrin-Based MOFs. *J. Am. Chem. Soc.* **2011**, *133*, 15858−15861.

(24) Ma, X.; Kang, J.; Wu, Y.; Pang, C.; Li, S.; Li, J.; Xiong, Y.; Luo, J.; Wang, M.; Xu, Z. Recent Advances in Metal/Covalent Organic Framework-Based Materials for Photoelectrochemical Sensing Applications. *Trends Anal. Chem.* **2022**, *157*, No. 116793.

(25) Wang, Q.; Astruc, D. State of the Art and Prospects in Metal-Organic Framework (MOF)-Based and MOF-Derived Nanocatalysis. *Chem. Rev.* **2020**, *120*, 1438−1511.

(26) Liu, T.; Tao, Q.; Wang, Y.; Luo, R.; Ma, J.; Lei, J. Tailored Cis−Trans Isomeric Metal−Covalent Organic Frameworks for Coordination Configuration-Dependent Electrochemi-luminescence. *J. Am. Chem. Soc.* **2024**, *146*, 18958−18966.

(27) Zhang, M.; Wang, J.; Xue, H.; Zhang, J.; Peng, S.; Han, X.; Deng, Y.; Hu, W. Acceptor-Doping Accelerated Charge Separation in Cu_2O Photocathode for Photoelectrochemical Water Splitting: Theoretical and Experimental Studies. *Angew. Chem., Int. Ed.* **2020**, *59*, 18463−18467.

(28) Zhang, T.; Hou, Y.; Dzhagan, V.; Liao, Z.; Chai, G.; Löffler, M.; Olianas, D.; Milani, A.; Xu, S.; Tommasini, M.; Zahn, D. R. T.; Zheng, Z.; Zschech, E.; Jordan, R.; Feng, X. Copper-Surface-Mediated Synthesis of Acetylenic Carbon-Rich Nanofibers for Active Metal-Free Photocathodes. *Nat. Commun.* **2018**, *9*, No. 1140.

(29) Luo, R. G.; Luo, X.; Xu, H. C.; Wan, S. S.; Lv, H. F.; Zou, B. E.; Wang, Y. F.; Liu, T. R.; Wu, C.; Chen, Q. Z.; Yu, S. Q.; Dong, P. F.; Tian, Y. X.; Xi, K.; Yuan, S.; Wu, X. J.; Ju, H. X.; Lei, J. P. Reticular Ratchets for Directing Electrochemiluminescence. *J. Am. Chem. Soc.* **2024**, *146*, 16681−16688.

(30) Bi, S.; Yang, C.; Zhang, W.; Xu, J.; Liu, L.; Wu, D.; Wang, X.; Han, Y.; Liang, Q.; Zhang, F. Two-Dimensional Semiconducting Covalent Organic Frameworks Via Condensation at Arylmethyl Carbon Atoms. *Nat. Commun.* **2019**, *10*, No. 2467.

(31) Balog, Á.; Kecsenovity, E.; Samu, G. F.; He, J.; Fekete, D.; Janáky, C. Paired Photoelectrochemical Conversion of CO_2/H_2O and Glycerol at High Rate. *Nat. Catal.* **2024**, *7*, 522−535.

(32) Xu, Q.; Zhang, L.; Cheng, B.; Fan, J.; Yu, J. S-Scheme Heterojunction Photocatalyst. *Chem.* **2020**, *6*, 1543−1559.

(33) Chen, R. F.; Wang, Y.; Ma, Y.; Mal, A.; Gao, X. Y.; Gao, L.; Qiao, L. J.; Li, X. B.; Wu, L. Z.; Wang, C. Rational Design of Isostructural 2D Porphyrin-based Covalent Organic Frameworks for Tunable Photocatalytic Hydrogen Evolution. *Nat. Commun.* **2021**, *12*, No. 1354.

(34) Xu, W. J.; Huang, B. X.; Li, G.; Yang, F.; Lin, W.; Gu, J. X.; Deng, H. G.; Gu, Z. G.; Jin, H. G. Donor−Acceptor Mixed-

Naphthalene Diimide-Porphyrin MOF for Boosting Photocatalytic Oxidative Coupling of Amines. *ACS Catal.* **2023**, *13*, 5723−5732.

(35) Zhang, X.; Li, Z.; Zeng, B.; Li, C.; Han, H. EPR Study of Charge Separation Associated States and Reversibility of Surface Bound Superoxide Radicals in $SrTiO_3$ Photocatalyst. *J. Energy Chem.* **2022**, *70*, 388−393.

(36) Huang, J. S.; Goh, T.; Li, X.; Sfeir, M. Y.; Bielinski, E. A.; Tomasulo, S.; Lee, M. L.; Hazari, N.; Taylor, A. D. Polymer Bulk Heterojunction Solar Cells Employing Forster Resonance Energy Transfer. *Nat. Photonics* **2013**, *7*, 479−485.

(37) Gupta, V.; Bharti, V.; Kumar, M.; Chand, S.; Heeger, A. J. Polymer−Polymer Förster Resonance Energy Transfer Significantly Boosts the Power Conversion Efficiency of Bulk-Heterojunction Solar Cells. *Adv. Mater.* **2015**, *27*, 4398−4404.

(38) Cai, P.; Xu, M.; Meng, S. S.; Lin, Z.; Yan, T.; Drake, H. F.; Zhang, P.; Pang, J.; Gu, Z. Y.; Zhou, H. C. Precise Spatial-Designed Metal-Organic-Framework Nanosheets for Efficient Energy Transfer and Photocatalysis. *Angew. Chem., Int. Ed.* **2021**, *60*, 27258−27263.

(39) Dolgopolova, E. A.; Williams, D. E.; Greytak, A. B.; Rice, A. M.; Smith, M. D.; Krause, J. A.; Shustova, N. B. A Bio-inspired Approach for Chromophore Communication: Ligand to-Ligand and Host-to-Guest Energy Transfer in Hybrid Crystalline. *Angew. Chem., Int. Ed.* **2015**, *54*, 13639−13643.

(40) Liu, H. X.; Si, D. H.; Smith, M. F.; Li, R. F.; Li, X. Y.; Li, L.; Huang, H. B.; Fang, Z. B.; Zhou, H. C.; Liu, T. F. Efficient CO_2 Photoreduction Enabled by the Energy Transfer Pathway in Metal-Organic Framework. *Aggregate* **2023**, *4*, No. e383.

(41) Fiankor, C.; Nyakuchena, J.; Khoo, R.; Zhang, X.; Hu, Y.; Yang, S.; Huang, J.; Zhang, J. Symmetry-Guided Synthesis of N,N'-Bicarbazole and Porphyrin-Based Mixed-Ligand Metal−Organic Frameworks: Light Harvesting and Energy Transfer. *J. Am. Chem. Soc.* **2021**, *143*, 20411−20418.

(42) Xiong, Z.; Li, Y.; Yuan, Z.; Liang, J.; Wang, S.; Yang, X.; Xiang, S.; Lv, Y.; Chen, B.; Zhang, Z. Switchable Anisotropic/Isotropic Photon Transport in a Double-Dipole Metal−Organic Framework via Radical-Controlled Energy Transfer. *Adv. Mater.* **2024**, *36*, No. 2314005.

(43) Cao, Y.; Huang, Y.; Zheng, J.; Chen, J.; Zeng, B.; Cheng, X.; Wu, C.; Wang, J.; Tang, J. Bipolar Photoelectrochemistry for Phase-Modulated Optoelectronic Hybrid Nanomotor. *J. Am. Chem. Soc.* **2024**, *146*, 17931−17939.

(44) Moghadam, F. M.; Rahaie, M. A Signal-on Nanobiosensor for $VEGF_{165}$ Detection Based on Supraparticle Copper Nanoclusters Formed on Bivalent Aptamer. *Biosens. Bioelectron.* **2019**, *132*, 186−195.

(45) Fan, J.; Tang, Y.; Yang, W.; Yu, Y. Disposable Multiplexed Electrochemical Sensors Based on Electro-Triggered Selective Immobilization of Probes for Simultaneous Detection of DNA and Proteins. *J. Mater. Chem. B* **2020**, *8*, 7501−7510.

(46) Kong, W. S.; Xu, Z. Y.; Liu, T. R.; Lei, J. P.; Ju, H. X. Photocurrent Polarity Reversal Induced by Electron-Donor Release for the Highly Sensitive Photoelectrochemical Detection of Vascular Endothelial Growth Factor 165. *Anal. Chem.* **2023**, *95*, 16392−16397.

(47) Zhang, H.; Li, M.; Li, C.; Guo, Z.; Dong, H.; Wu, P.; Cai, C. G-quadruplex DNAzyme-based Electrochemi-luminescence Biosensing Strategy for $VEGF_{165}$ Detection: Combination of Aptamer-Target Recognition and T7 Exonuclease-Assisted Cycling Signal Amplification. *Biosens. Bioelectron.* **2015**, *74*, 98−103.

(48) Zhong, Y.; Zha, R.; Li, W.; Lu, C.; Zong, Y.; Sun, D.; Li, C.; Wang, Y. Signal-On Near-Infrared Photoelectrochemical Aptasensors for Sensing $VEGF_{165}$ Based on Ionic Liquid-Functionalized Nd-MOF Nanorods and In-Site Formation of Gold Nanoparticles. *Anal. Chem.* **2022**, *94*, 17835−17842.

https://doi.org/10.1021/jacs.5c07699